Acta Biomaterialia 184 (2024) 461–472

Contents lists available at ScienceDirect

Acta Biomaterialia

journal homepage: www.elsevier.com/locate/actbio

Full length article

Assessment of tissue response *in vivo*: PET-CT imaging of titanium and biodegradable magnesium implants

Leon Riehakainen[a,b,*], Eduarda Mota-Silva[a,b], Claudia Kusmic[b], Daniele Panetta[b], Debora Petroni[b], Davide Fragnito[b], Stefano Salvadori[b], Luca Menichetti[b]

[a] The Sant'Anna School of Advanced Studies, Pisa, Italy
[b] Institute of Clinical Physiology, National Research Council (IFC-CNR), Pisa, Italy

ARTICLE INFO

Article history:
Received 19 January 2024
Revised 1 June 2024
Accepted 6 June 2024
Available online 11 June 2024

Keywords:
PET
Biodegradable magnesium
Implants
Biocompatibility
In vivo imaging
Inflammation
Osteogenesis
Angiogenesis

ABSTRACT

To study *in vivo* the bioactivity of biodegradable magnesium implants and other possible biomaterials, we are proposing a previously unexplored application of PET-CT imaging, using available tracers to follow soft tissue and bone remodelling and immune response in the presence of orthopaedic implants. Female Wistar rats received either implants (Ti6Al7Nb titanium or WE43 magnesium) or corresponding transcortical sham defects into the diaphyseal area of the femurs. Inflammatory response was followed with [^{18}F]FDG and osteogenesis with [^{18}F]NaF, over the period of 1.5 months after surgery. An additional pilot study with [^{68}Ga]NODAGA-RGD tracer specific to $\alpha_v\beta_3$ integrin expression was performed to follow the angiogenesis for one month.

[^{18}F]FDG tracer uptake peaked on day 3 before declining in all groups, with Mg and Ti groups exhibiting overall higher uptake compared to sham. This suggests increased cellular activity and tissue response in the presence of Mg during the initial weeks, with Ti showing a subsequent increase in tracer uptake on day 45, indicating a foreign body reaction. [^{18}F]NaF uptake demonstrated the superior osteogenic potential of Mg compared to Ti, with peak uptake on day 7 for all groups. [^{68}Ga]NODAGA-RGD pilot study revealed differences in tracer uptake trends between groups, particularly the prolonged expression of $\alpha_v\beta_3$ integrin in the presence of implants.

Based on the observed differences in the uptake trends of radiotracers depending on implant material, we suggest that PET-CT is a suitable modality for long-term *in vivo* assessment of orthopaedic biomaterial biocompatibility and underlying tissue reactions.

Statement of significance

The study explores the novel use of positron emission tomography for the assessment of the influence that biomaterials have on the surrounding tissues. Previous related studies have mostly focused on material-related effects such as implant-associated infections or to follow the osseointegration in prosthetics, but the use of PET to evaluate the materials has not been reported before. The approach tests the feasibility of using repeated PET-CT imaging to follow the tissue response over time, potentially improving the methodology for adopting new biomaterials for clinical use.

1. Introduction

The increasing interest in biodegradable implants in recent years has resulted in the development of a wide range of potentially suitable materials. Metals, polymers and ceramics include materials that can naturally disappear after their role has been completed, thus avoiding further patient discomfort or complications that may lead to implant removal surgeries increasing healthcare costs and health hazards for the patients. While traditional permanent implants, for example made from titanium or stainless steel, are focused on bioneutrality and corrosion resistance, they still carry with them the risk of stress shielding effect due to the differences in Young's modulus [1] and other complications such as chronic inflammation and undesired attachment between implant surfaces and mobile soft tissues such as tendons [2]. The

* Corresponding author.
E-mail address: leon.riehakainen@hotmail.com (L. Riehakainen).

https://doi.org/10.1016/j.actbio.2024.06.005

biodegradable implants become a part of the body's metabolism as the implant components react with the surrounding tissues, and are heavily dependent on their component materials that can affect the body by acting together or separately in a dose-dependent way. The need to ensure the safety of degradation products and reasonable degradation rate while maintaining the desired mechanical properties is one of the challenges in the field.

One of the promising materials is magnesium, a metal naturally present as a microelement in the human body [3] that has been used as implant material since the 19th century. As its Young's modulus is close to cortical bone (5–23 GPa) [4], it is attractive for orthopaedic use due to the reduced risk of stress shielding. Research has also produced results, suggesting the beneficial effect of magnesium on tissue healing. Notably the release of Mg^{+} ions has been reported to participate in multiple molecular and cellular mechanisms regulating inflammatory response and tissue regeneration [5], positively affecting blood vessel and new bone formation [6,7]. At the same time, magnesium is highly reactive, causing rapid degradation and gas release, which limited the application of magnesium in clinical use [8]. To deal with this and adjust mechanical properties, magnesium can be alloyed with aluminium (Al), zinc (Zn), calcium (Ca), copper (Cu), manganese (Mn) and lithium (Li), and also rare earth metals such as yttrium (Y) and gadolinium (Gd) [9–11]. However, such additives can be toxic at high concentrations or cause allergic reactions [10].

It is therefore unavoidable that a large number of material combinations, alloys and surface treatments are developed in an attempt to combine biocompatibility with the other desired properties suitable for specific application. The current methods of implant assessment are limited in long-term *in vivo* evaluations. Positron emission tomography with computed tomography (PET-CT) is an established method for *in vivo* metabolic imaging with anatomical registration. While optical imaging methods like photoacoustic imaging (PAI) can also image specific molecular targets, they are limited in imaging depth and area. For implant imaging, PET-CT has the advantage of being non-magnetic and universal, avoiding the imaging artefacts, risk of heating or implant movement that complicates the imaging of ferromagnetic materials with magnetic resonance imaging (MRI). Being non-invasive, PET-CT is well suitable for repeated use during the extended period of observation necessary for biodegradable implants. A large variety of radiotracers has been developed for specific biomarkers, providing options for targeting selected metabolic activity pathways, including inflammation, bone regeneration and neoangiogenesis [12].

In this study we used a rat model to explore the previously unstudied potential of using PET-CT with [^{18}F]FDG and [^{18}F]NaF tracers for evaluation of differences in inflammation and bone mineralization linked to the presence of magnesium or titanium implants with sham defect as a control. The aim of this study is to test the capacity of PET-CT imaging modality to detect and differentiate the possible long-term metabolic changes caused by implant materials and interpret the results based on the current understanding of the tissue response.

[^{18}F]FDG is a long-established tracer for imaging inflammatory reactions. As a glucose analogue, it participates in the glycolytic pathway and accumulates in the regions of increased metabolic activity. Abnormal cellular metabolism highlighted by tracer uptake can be associated with inflammatory reaction, infections and tumours [13,14]. In case of orthopaedic implants, [^{18}F]FDG has previously been used to study implant-related osteomyelitis and infections [15,16], with studies giving varied results in efficiency of diagnosing periprosthetic joint infections [17,18].

[^{18}F]NaF is the tracer suitable for studying bone growth and mineralization, and has been used to study bone pathologies, malignancies [19] and fracture healing [13]. In a study by Cofano et al. (2022), [^{18}F]NaF was used to successfully indicate the osseointegration of trabecular titanium cages during lumbar arthrodesis [20], supporting the idea of using the tracer for implant assessment studies. The tracer action mechanism relies on fluoride ion (F^{-}). It binds with hydroxyapatite to form fluorapatite on mineralizing newly formed bone according to the formula [19,21]

$$Ca_5(PO_4)_3OH + F^{-} \rightarrow Ca_5\ (PO_4)_3\ F + OH^{-}$$

The downside of [^{18}F]NaF is ion bonding to dead bone and calcium phosphate materials [22]. This can cause mistaken evaluation if bone particles remain in the wound.

Additionally, a limited pilot study was performed with [^{68}Ga]NODAGA-RGD tracer to evaluate angiogenesis. The peptide component, arginylglycylaspartic acid (RGD), binds to $\alpha_v\beta_3$ integrin, known for its role in new blood vessel formation [23–27]. However, $\alpha_v\beta_3$ integrin has also been found to be expressed by osteoclasts [28,29], which may result in false interpretation due to their active role in bone remodelling phase during normal healing and in bone resorption in case of complications such as osteomyelitis [30] or stress shielding [31].

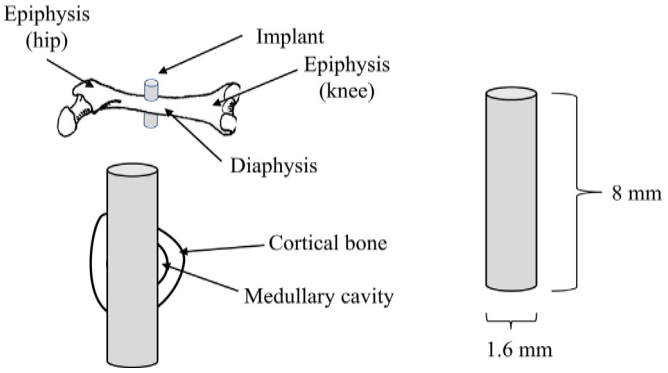

Fig. 1. Implant dimensions and target site. The implant dimensions allow reliable implantation into the diaphyseal area and sufficient contact with surrounding soft tissues to promote peri–implant interaction.

Table 1
Ti6Al7Nb titanium alloy composition by manufacturer.

Element	% w
Titanium	bulk
Aluminium	5.5–6.50
Niobium	6.5–7.50
Iron	< 0.25
Oxygen	< 0.13
Carbon	< 0.08
Nitrogen	< 0.05

2. Material and methods

2.1. Implants

Implants used were in the shape of 1.6 × 8 mm cylindrical pins (Fig. 1) produced from Ti6Al7Nb titanium (purchased from Medical University of Graz, Graz, Austria and manufactured by Acnis International, France) and WE43 magnesium alloy (Syntellix AG, Hannover, Germany).

The compositions of the alloys as reported by manufacturers are presented in Tables 1 and 2.

2.2. Animals

Female Wistar rats were purchased from Envigo RMS s.r.l. (S. Pietro al Natisone, Udine Italy), and after a week of quarantine

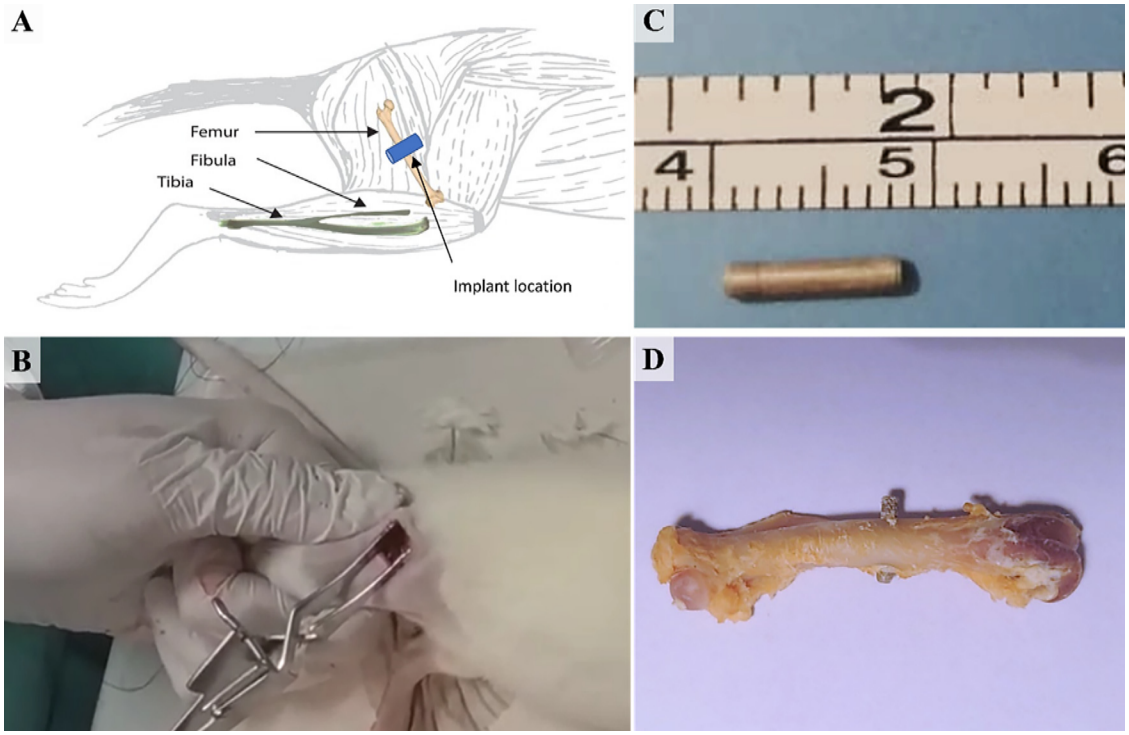

Fig. 2. Implantation site location in schematic (A) and during surgery with spread femoris muscles (B). WE43 implant before implantation (C) and in ex vivo extracted sample (D). Schematic drawing (A) from Nijhuis et al. (2013) [32] reproduced under Creative Commons Attribution 4.0 International (CC BY) licence.

Table 2
WE43 magnesium alloy composition by manufacturer.

Element	% w
Magnesium	85.20–95.89
Rare Earth content	2.50–5.00
Yttrium	1.50–5.00
Zirconium	0.10–2.50
Zinc	0.01–0.80
Total possible impurities	< 1.00
Aluminum as impurity	< 0.50

were 10–13 weeks old at the beginning of the experiment. Animals were housed in plastic cages with well-ventilated stainless steel grid tops, lined with wood chip bedding and equipped with cardboard and acrylic hiding tunnels. The housing room was maintained at steady temperature (21±0.5 °C) and humidity (55±2 %), with 12 h light/dark cycles. Upon arrival, rats were acclimatised for two weeks and fed standard chow (StD, Teklad Global 16 % Protein Rodent Diet, Envigo, Udine, Italy) and supplied with tap water *ad libitum*. Animals were kept in cages in pairs, except for the suture healing period after surgery. A total of 84 rats were operated for longitudinal study, with the aim to have $n = 10$ samples per implant group. Exclusion criteria included bone fracture and lameness (due to accidental sciatic nerve damage). While the bilateral surgery provided two samples per animal, the study interruptions during 2020–2021 pandemic required additional surgeries to ensure sufficient number of samples for later time points.

2.3. Surgery

Implantation surgery was performed under general anaesthesia/analgesia using Zoletil (zolazepam + tiletamine) 10 mg/kg (Virbac, Switzerland) + Xylazine 5 mg/kg (Rompun Elanco, Italy) administered intraperitoneally.

Before surgery, the lateral side of the animal's posterior legs were shaved using a depilatory cream (Veet, Reckitt Benckiser Healthcare S.p.A., Italy) and carefully cleaned to avoid skin burns from contact with the cream. The anaesthetised animal was placed on a heated platform on its left side.

The surgery area was cleaned with 70 % ethanol and an incision was made perpendicular to the femur shaft in mid-diaphysis area. All skin layers were cut through and femoris muscle tissues were carefully spread apart to expose the diaphyseal region of the femur (Fig. 2).

The bone was cleaned from soft tissue with a sterilised cotton tip and a 1.55 mm diameter drill was used to create a transcortical hole on the femur. A low drilling rotational speed was selected, and physiological saline (Fresenius Kabi, Italy) was dripped to minimise frictional heat and thermal damage to the tissue.

The implant was inserted by gentle tapping, resulting in a uniform press fit. After pin placement, the wound site was cleaned with sterile cotton tips for remaining bone debris and the wound was closed with white resorbable sutures (Johnson & Johnson Medical, Italy). The contralateral hindlimb was operated similarly and using the same implant type. Sham surgery was conducted identically to the implantation procedure, with the exception of implant insertion, resulting in a naturally healing defect.

Animals were injected intraperitoneally with 0.1 ml of Ketorolac and left to wake up in their individual cages under an infrared lamp to avoid hypothermia. The animals were kept under observation until awakening and resumption of the basic physiological activities.

Postoperatively, additional prophylactic painkiller Ketorolac (6 mg/kg) was also administered via intraperitoneal injection. Antibiotic (Baytril 5 mg/100 ml) and painkiller (Tramadol 3 mg/100 ml) were supplied with the drinking for a week fol-

Table 3
PET acquisition settings in IRIS PET/CT used in the study.

PET acquisition protocol	
Acquisition Time (sec)	900
Number of bed positions	1
PET preprocessing protocol	
Frame Protocol	3 by 300 s each
Energy Window (keV)	350–750
Corrections	Decay, Dead Time, Randoms
Gating	No cardiac/respiratory gating
PET reconstruction protocol	
Algorithm	3D-OSEM-MC
Subsets	8
Iterations	8
Voxel Size	Standard
Normalization	Yes
Attenuation Correction	Yes
Quantitative Image	Yes

Table 4
CT acquisition settings in IRIS PET/CT used in the study.

CT acquisition protocol	
Frames	1
Number of bed positions	1
Scan Type	Full Scan
Tube Voltage (kV)	80
Tube Current	Full (Low Noise)
Number of Projections	800
Exposure Time (ms)	50
Rotation Type	Continuous
Sensitivity Mode	Standard
CT preprocessing protocol	
Voxel Size	120 µm
Transversal FOV	Full FOV
Axial FOV	100 %
Respiratory Gating	No
CT reconstruction protocol	
Filter Window	Normal
Voxel Size	Standard
Beam Hardening Correction	Yes
Ring Artifact Pre-Correction	Yes
Ring Artifact Post-Correction	No

lowing the surgery. Regular observations of gait, posture and behaviour revealed no discomfort that implants could have caused to the animals.

2.4. PET-CT

Animals with titanium or magnesium implants or sham defects were imaged on days 1, 3, 7, 14, 28 and 45 after surgery with [^{18}F]FDG and [^{18}F]NaF tracers or on days 7, 15 and 32 with [^{68}Ga]NODAGA-RGD tracer. The injected activity was ca 14 MBq for [^{18}F]-isotope containing tracers and ca 18 MBq for [^{68}Ga]NODAGA-RGD.

Imaging was performed using IRIS PET/CT (Inviscan Imaging System, Strasbourg, France) [33,34], acquisition settings are outlined in Tables 3 and 4.

For tracer injection and imaging, animals underwent inhalation anaesthesia with 5 % induction and 2.5 % maintenance isoflurane concentration with oxygen flow of around 3l/min (vaporizer Fortec 3, Cyprane Ltd). After injection, animals were left to recover in their cages in lead-lined cabinet under infrared lamp. 60 min after tracer injection, animals were imaged with PET for 15 min (3 × 5 min frames).

A Medical Image Data Examiner (AMIDE) was used for image analysis. Implants or sham defect sites were located using CT modality to assist in drawing volumes of interest (VOIs). The VOIs were designed to cover the region affected by the implantation, defined by the extent of damage during surgery and observation of increased tracer uptake region during the early stage of the study. For [^{18}F]FDG and [^{68}Ga]NODAGA-RGD, 4.8 × 8 mm cylindrical VOI was centred over the implant or in the case of sham group, over the defect, aiming to centre it along the drilled defect axis. For [^{18}F]NaF, 4.8 × 4 mm VOI was drawn axially centred on the implant and transaxially covering the bone. PET VOI data were exported into Excel document for further analysis. The median VOI concentration values were all corrected using linear estimation to represent the tracer activity concentration at 60 min after injection and standardised uptake values (SUVs) were calculated. The resulting values were plotted using OriginPro Version 2022 (OriginLab Corporation, Northampton, MA, USA).

2.5. Implant material attenuation test

In order to test the magnitude of the effect that the difference in linear absorption coefficients of magnesium and titanium implants have on PET acquisition, preliminary testing was performed *ex vivo*. The extracted rat femurs, with magnesium or titanium pins implanted as in the main study, were placed in 15 ml Falcon tubes. The same volume and concentration of [^{18}F]FDG was added into both Falcon tubes and imaged at the settings of the main study (Tables 3 and 4), except that acquisition was set to one 5-minute frame. Samples were imaged together and separately.

The resulting images were analysed with the main study [^{18}F]FDG workflow with the same VOIs applied. The results showed a max 0.27 % difference between the median concentration values of the magnesium and titanium sample VOIs, but 12.7 % between mean values. Samples with titanium implants also had much higher variation (115.85 %), standardised deviation (63.3 %) and maximum (63.91 %) values. Based on these results, median values were consequently used in main study PET-CT calculations and statistics.

2.6. Statistical analysis

For statistical calculations, the acquired values were analysed using a generalised additive model (GAM) to compensate for the data not fitting both linearity and normality assumption and also being intermittent due to interruptions caused by global pandemic during the experimental phase of the project.

GAM, an expansion of the general linear model (GLM) can be used to generalise a general linear model by allowing additivity of non-linear functions of the variables [35]. Calculations were performed in R software (Core Team (2018). R: A language and environment for statistical computing. R Foundation for Statistical Computing, Vienna, Austria) defined using the bam() function from the mgcv package.

Sensitivity analysis was conducted to include different random effects into the model. The performance of each of them was evaluated over different statistical parameters to pick the optimal choice. These included Akaike's Information Criterion (AIC), second-order (or small sample) AIC with a correction for small sample sizes (AICc), Bayesian Information Criterion (BIC), r-squared value (R2), root mean squared error (RMSE) and residual standard deviation (Sigma).

The model utilises the SUV values as the outcome variable and represents them as a function of two predictor variables: treatment and a random smooth function of day. These predictors are further defined through the interaction of the implant group (Mg, Ti, and sham) and the site of implantation (hindlimb laterality delineated

as “left” or “right” legs). This is defined using random smooth interactions [36]. The primary objective of the model is to accurately capture the curve that describes the relationship between the response values and the remaining variables in the formula. This includes accounting for non-linear and visually observed non-monotonic relationships that may exist over time between treatments and variations in laterality (left or right legs). To address all inquiries, pairwise contrasts were conducted using marginal contrast analysis. To estimate individual pairwise contrasts across implants and contrasts for each time point within the study group, the estimate_contrasts function from the "modelbased" package in R was utilised.

To reduce type I error, all pairwise contrasts considered are adjusted following the false discovery rate procedure (FDR) [37], with alpha significance level of 0.05.

Prior to analysing the statistical model, a preliminary step was taken to identify one-dimensional outliers within the dataset. These outliers were identified regardless of the relationships between variables, instead, they were grouped based on the implant group and the day of observation, automating these steps of the procedure. The identification of outliers was facilitated using the "identify_outliers" function available in the rstatix statistical package in R.

2.7. Histology

To confirm and evaluate the differences in effects that the implant materials have on tissue healing and response, randomly chosen animals from each group were euthanised for qualitative assessment. The extracted femur diaphysis from rat specimens were immersed in 10 % neutral-buffered formalin for a minimum of 72 h to achieve fixation and processed for histology using haematoxylin and eosin (HE) and Levai-Laczko staining.

For on-site HE staining, the samples were rinsed under running tap water for approximately 10–15 min, and the bones underwent decalcification for a duration of 4 weeks using a 12 % EDTA solution (pH 7.4) (Osteodec from Bio Optica, Milan, Italy). Solution was changed weekly, and the decalcification process was monitored. Once the bones attained a slightly elastic texture after a few days, the implants were delicately extracted, and the bones fully decalcified.

The samples were then rinsed under running tap water for 15 min, and the standard dehydration procedure was carried out using a series of gradually increasing ethanol solutions (70 % overnight, 80 % for 40 min, 96 % for 40 min, and three cycles of 100 % for 40 min each). Subsequently, the samples were immersed in xylene for three cycles of 40 min each, and then embedded in paraffin through four 40-minute cycles. Tissue sections were produced using a rotary microtome.

The deparaffinization was done by treating with xylene for 20 min, followed by 100 % and 96 % ethanol for 10 min each and subsequent 5–10 min rehydration in distilled water. The sections, with a thickness of 5 µm, were stained with Mayer’s haematoxylin solution for 5 min, rinsed in running tap water for 10 min, and then stained in eosin Y aqueous solution for 2 min. The slides were rinsed in distilled water, dehydrated quickly using graded alcohol, cleared with xylene, and permanently mounted on slides.

Levai-Laczko staining was outsourced (LLS ROWIAK LaserLabSolutions GmbH, Germany). The formalin-fixed samples were dehydrated in a grade series of alcohol and embedded in methylmethacrylate (MMA)(Technovit 9100 neu, Kulzer, Germany). Laser microtome (TissueSurgeon, LLS ROWIAK LaserLabSolutions, Hannover, Germany) was used to section samples lengthwise, to a thickness of approximately 10 µm. The samples were stained and mounted on slides.

Histological images were captured using a light microscope (Olympus BX43, Japan) and digitised using an RGB video camera (Olympus DP 20, Japan).

3. Results

With [^{18}F]FDG, a total of 37 (n = 15 Mg, 15 Ti, 7 sham) and with [^{18}F]NaF, a total of 23 (n = 8 Mg, 9 Ti, 6 sham) animals were imaged and analysed. For pilot study with [^{68}Ga]NODAGA-RGD, a total of 6 (n = 2 Mg, 2 Ti, 2 sham) animals were imaged and analysed. Example images for tracers and implants acquired on highest SUV days are presented in Fig. 3.

3.1. [^{18}F]FDG tracer uptake

With alpha value 0.05, statistically significantly different uptake of [^{18}F]FDG between compared pairs was found to be as follows (Fig. 4):

- Mg vs Ti: Mg implant group had higher uptake than Ti group on day 7.
- Mg vs sham: Mg group showed higher uptake than sham group from day 1 to 14.
- Ti vs sham: Ti group had higher uptake than sham group on days from 1 to 7, and on days 28–45.

The performance analysis of the GAM model (Supplementary Figure 1.D) validated the use of the model. The laterality had an insignificant effect on the results (Supplementary Figure 1.B), suggesting that there was little effect on the results caused by mechanical loading differences from the dominant limb. However, the diagnostic plot expressing the difference between residuals against linear prediction (Supplementary Figure 1.C) showed a horizontal cone trend, indicating heteroskedasticity of residuals in the model. This is likely due to limited sample pool, related to interruptions in imaging schedule.

3.2. [^{18}F]NaF tracer uptake

The pairwise comparison analysis showed statistically significantly different tracer uptake (with alpha value 0.05) between compared pairs (Fig. 5) was found to be:

- Mg vs Ti: Mg implant resulted in higher SUVs than Ti from day 7 to 28.
- Mg vs sham: Mg group’s tracer uptake was above sham from day 1 to 28.
- Ti vs sham: Ti implant group had higher uptake than sham from day 1 to 7.

The GAM performance values (Supplementary Figure 2.D) also validated the performance of the model for [^{18}F]NaF tracer data. The laterality had likewise insignificant effect on the uptake of the tracer (Supplementary Figure 2.B). The diagnostic plot for the differences between the residuals and linear prediction (Supplementary Figure 2.C) similarly produced a horizontal cone trend implying a heteroskedasticity of residuals in the model. As was in the case of [^{18}F]FDG results, this is likely due to interruptions in imaging schedule and resulting limited sample pool.

3.3. [^{68}Ga]NODAGA-RGD tracer uptake

The SUV results are plotted in Fig. 6 below, showing different dynamics of tracer uptake over time between groups. Notably, SUVs for sham injury group on day 15 have sharply declined, reaching the level similar to the values on day 32. That is different from implant groups, where the values remain elevated from day 7 to 15. Because of the limited number of samples in this pilot study, no statistical analysis was performed.

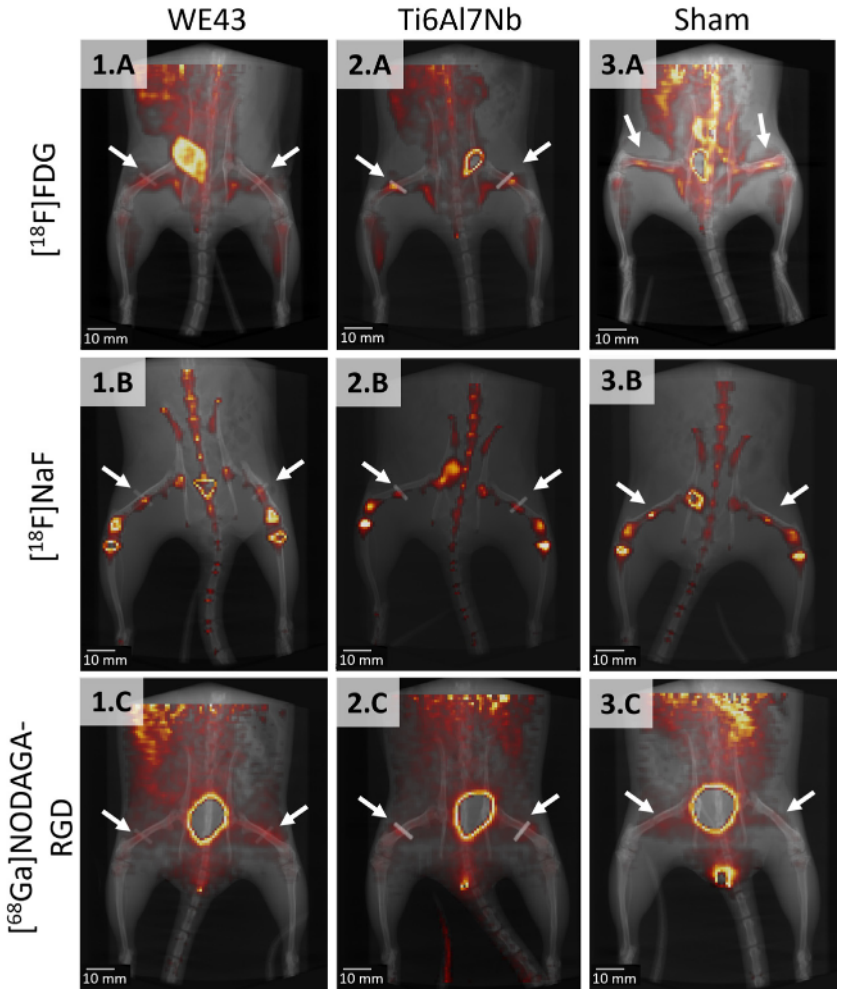

Fig. 3. Distribution of [^{18}F]FDG on day 3 (A), [^{18}F]NaF (B) and [^{68}Ga]NODAGA-RGD (C) on day 7 after surgery. Magnesium implants (1.A-C), titanium implants (2.A-C), sham defect (3.A-C). Implant and sham defect locations indicated with white arrows. Histograms have been individually adjusted to provide optimal view of uptake at the site of interest. All tracers showed increased uptake at the implant/defect site. In CT; magnesium implants show similar radiopacity to bone, while titanium is significantly more dense, which can result in characteristic streaks of beam hardening.

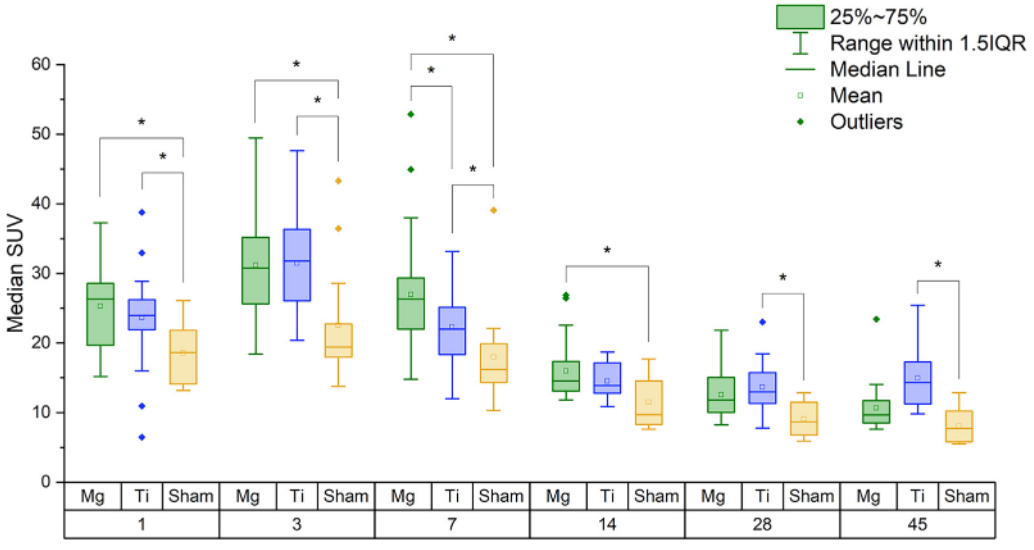

Fig. 4. [^{18}F]FDG PET results. Asterisks highlight statistically different group pairs within time point. For all groups, the tracer uptake peaks on day 3, and gradually reduces towards the end. Notably, titanium shows an increase in median SUVs on final time point, suggesting foreign body reaction.

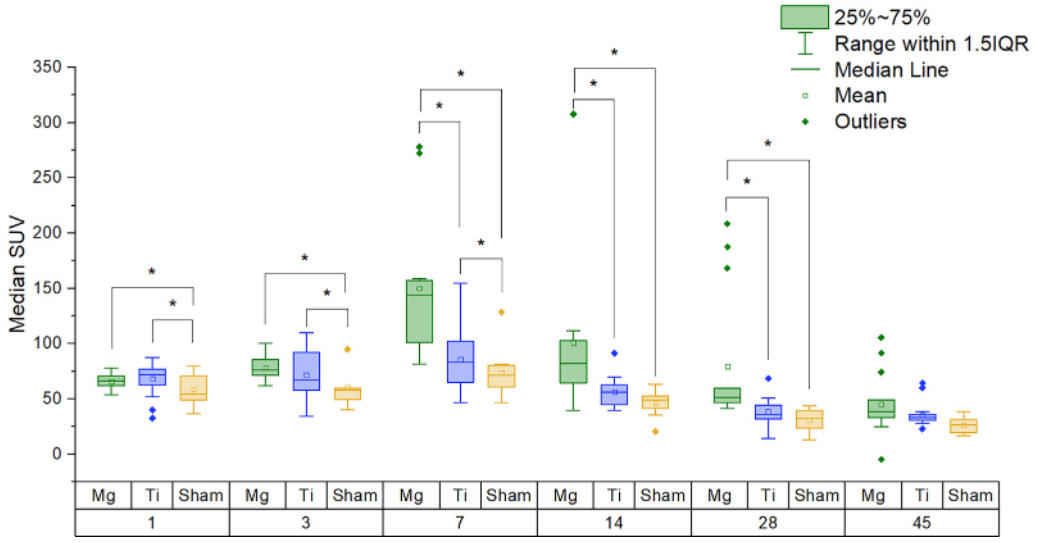

Fig. 5. [^{18}F]NaF PET results until day 45. Asterisks highlight statistically different group pairs within time a point. Tracer uptake for all groups peaks on day 7 when all groups show significant statistical differences, and then steadily decreases until there is no statistically significant difference between groups on day 45.

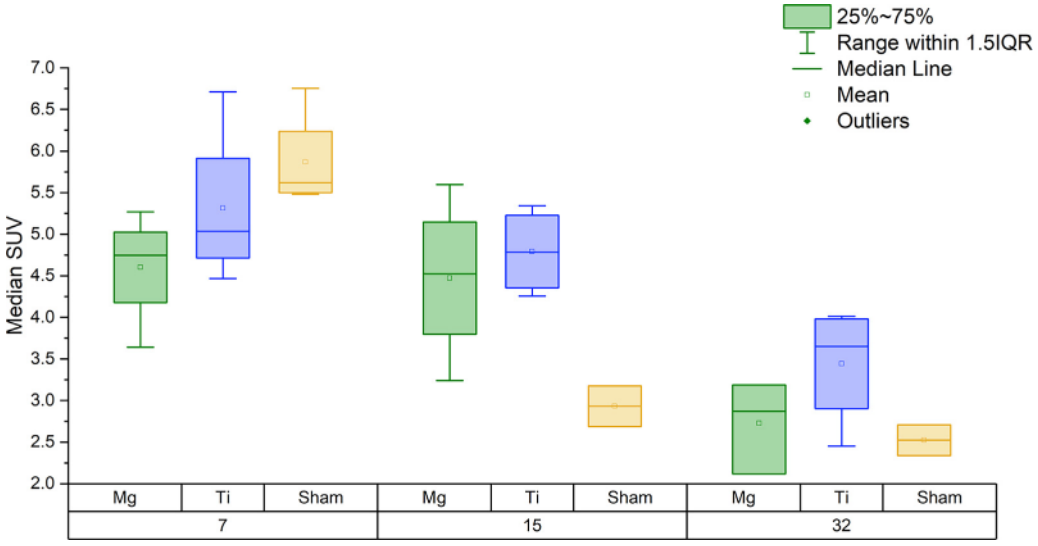

Fig. 6. Median VOI SUVs of [^{68}Ga]NODAGA-RGD on days 7, 15 and 32 after surgery. The tracer uptake for sham injury is distinctly different from implants, going from highest median SUVs between groups on day 7 to lowest on day 15.

3.4. Histological observations

The Levai-Laczko stained micrographs showing the in situ interaction between implants and bone are presented in Fig. 7. Additionally, the gas generated from the degradation of magnesium implants is prominent in the intramedullary cavity (Fig. 7.1.A), different from the dense cell aggregation that is otherwise seen around the titanium implant in Fig. 7.2.A.

The micrographs shown in Fig. 8, from decalcified samples with removed implants and stained with haematoxylin and eosin, focus on cellular response of the tissues. On day 7, the healing response in the presence of both magnesium and titanium implants primarily involves periosteal reaction. This response is characterised by the formation of new bone following the injury to the periosteum covering the bone at the implantation site. Both implants induce the development of reactive periosteal callus, consisting predominantly of chondrocytes, surface osteoblasts, and newly formed woven and lamellar bone (Fig. 8.1.B-C and 2.B). This increased bone formation could be one of the factors contributing to the elevated uptake of [^{18}F]FDG and [^{18}F]NaF observed in PET scans.

In the medullary cavity surrounding the magnesium implants (Fig. 8.1.), voids similar to those observed in Fig. 7.1. are present, resulting from the release of gas during the degradation of magnesium. However, the cellular composition of the region adjacent to the bone defect within the medullary cavity indicates an active bone repair process (Fig. 8.1.D), as mesenchymal osteoblasts are surrounded by a recognizable woven bone matrix.

In the micrographs of the medullary cavity surrounding the titanium implant (Fig. 8.2.A and 2.C), despite the presence of mesenchymal osteoblasts and the formation of new woven bone, the active healing processes occur further away from the immediate vicinity of the implant. Histological observations suggest that the titanium implant leads to the formation of a reactive vascularized connective tissue layer, isolating the implant from the bone (Fig. 8.2.D), previous studies have demonstrated that this may result in poorer long-term osseointegration of the Ti implant compared to the Mg pins [38–40].

Fig. 8.3 displays a sham injury at day 14, demonstrating a direct bone repair mechanism (gap repair) facilitated by marrow-derived vessels and mesenchymal osteoblasts, without involving a cartilage

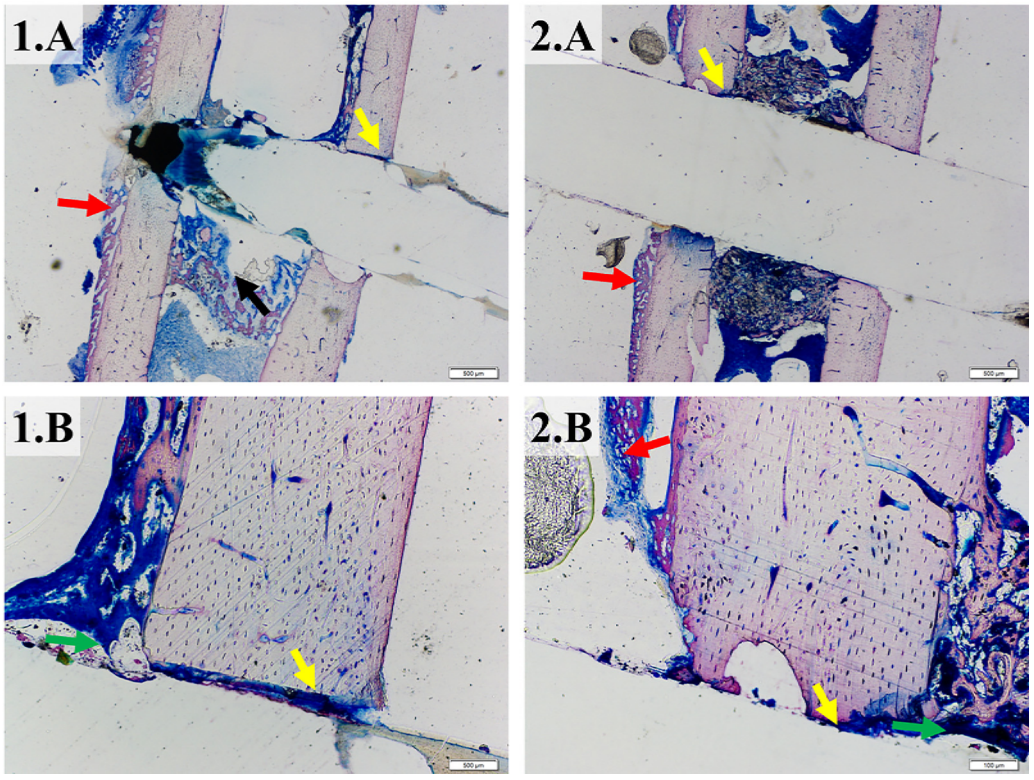

Fig. 7. Levai-Laczko staining of samples from day 7 after surgery for magnesium (1) and titanium (2) groups. Magnification set to 2x for A and 10x for B. Red arrows: soft callus formed around the implant and bone. Yellow arrows: implant-tissue contact. Green arrows: the contact of implants with the intramedullary cavity. Black arrow: gas cavities from Mg degradation.

phase. The bone defect is largely filled with newly formed woven bone (Fig. 8.3.C). The repair process originates from the marrow and extends toward the cortex by filling the defects.

Frames 1.A-D: Representative micrographs of bone tissue reactions in the presence of magnesium implant. Frame 1.A: image taken at 2x magnification through the entire implanted region (scale bar: 500 µm). Frames 1.B-C: Inset at 20x magnification (scale bar: 50 µm) shows the details of periosteal callus surrounding the pin. Frame 1.D: Inset at 20x magnification (scale bar: 50 µm) present the details of the medullary cavity. The defect edges are marked with blue dashed lines. Red arrows: mesenchymal osteoblast. Green arrows indicate surface osteoblasts. Black arrows: voids from gas released by magnesium degradation in the medullary cavity. BM: bone marrow; C: chondrocytes; G: gas bubble; L: lamellar bone; W: newly formed woven bone.

Frames 2.A-D: Representative micrographs of bone tissue reactions in the presence of titanium implant. Frame 2.A: image taken at 2x magnification through the entire implanted region (scale bar: 500 µm). Frame 2.B: Inset at 20x magnification (scale bar: 50 µm) shows the periosteal callus surrounding the pin. Frame 2.C: Inset at 10x magnification (scale bar: 100 µm) presents the details of medullary cavity. Frame 2.D: Inset at 40x magnification (scale bar 20 µm) demonstrates the reactive connective tissue grown between the bone surface and the titanium implant. The defect edges are marked with blue dashed lines. Green arrows: surface osteoblasts. Black arrows: red blood cells present into the reactive neovascularization. BM: bone marrow; C: chondrocytes; L: lamellar bone; W: newly formed woven bone.

Frames 3.A-C: Representative micrographs of bone tissue reactions to femoral defects in the sham group. Frame 3.A: image taken at 2x magnification through the entire defect region (scale bar: 500 µm). Frame 3.B: Inset at 10x magnification (scale bar: 100 µm) demonstrates an islet of newly formed woven bone (W). Frame 3.C: Inset at 40x magnification (scale bar: 20 µm) shows details of bone repair processes. The defect edges are marked with blue dashed lines. Black arrows: mesenchymal osteoblasts. BM: bone marrow; L: lamellar bone; W: newly formed woven bone.

The histological observations show that titanium implants develop a noticeable peri–implant layer, absent from magnesium samples, that can be indicative of fibrous capsule formation (Fig. 8.2.D). Both implants showed noticeable outside callus formation (Fig. 8.1-2), one of the possible reasons for increased [^{18}F]FDG and [^{18}F]NaF uptake observed in PET.

4. Discussion

The aim of the study was to investigate the use of PET imaging to analyse the metabolic changes caused by differences in implant material. Through monitoring the changes in radiotracer uptake, we were observing the tissue responses in the presence of biodegradable magnesium, permanent titanium and sham injury. The overview of statistical uptake differences between groups for [^{18}F]FDG and [^{18}F]NaF is presented in Table 5.

The summary of median SUVs and standard deviations in each experimental group is presented in Table 6.

The differences between implant groups had a common characteristic for both [^{18}F]FDG and [^{18}F]NaF tracers – in all statistically significantly different comparisons, magnesium implant samples had higher SUVs than titanium, which in turn had higher SUVs than sham operated controls. Significantly, the observed differences between implant groups were less compared to their contrast with sham. The increased uptake values of both tracers for magnesium may be attributed to its bioactivity and metabolic effects of Mg^{+} ions [5] combined with improved cell adhesion to implant surface due to the combination of corrosion layer composed of magnesium hydroxide and the additional deposition of

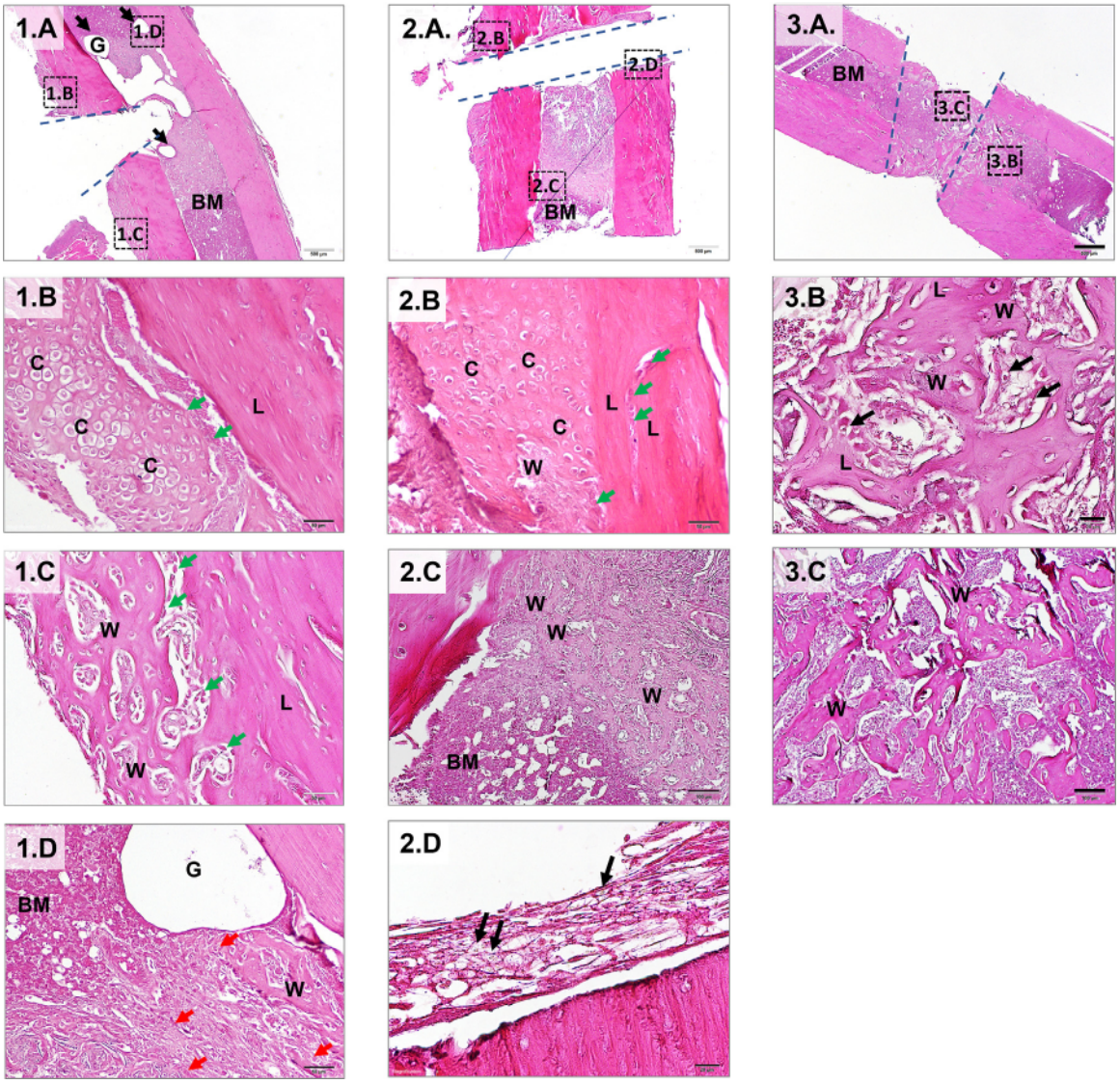

Fig. 8. HE staining of samples from day 7 for magnesium (Frame 1) and titanium (Frame 2) groups, and day 14 for sham injury (Frame 3).

Table 5
Tracer uptake contrasts between groups. Less (<) and greater (>) signs indicate the relationship between groups. 1 sign $P \leq 0.05$, 2 signs $P \leq 0.01$, 3 signs $P \leq 0.001$.

[^{18}F]NaF uptake differences between groups							
Group 1	Day 1	Day 3	Day 7	Day 14	Day 28	Day 45	Group 2
Mg			>>>	>>>	>>		Ti
Mg	>	>>>	>>>	>>>	>>		Sham
Ti	>>>	>>	>				Sham
[^{18}F]FDG uptake difference between groups							
Group 1	Day 1	Day 3	Day 7	Day 14	Day 28	Day 45	Group 2
Mg			>				Ti
Mg	>>>	>>>	>>>	>			Sham
Ti	>>>	>>>	>>>		>	>	Sham

phosphorus, calcium and proteins [41,42]. The osteogenic properties of magnesium have also been reported to result in better osseointegration of magnesium implants compared to titanium analogues [43], which was also observed in histological evidence. A study by Lindter et al. (2013) using undecalcified histology shows direct bone contact at day 30 (4 weeks) in a rodent model of femur diaphyseal transcortical implantation of a Mg-Y-Nd-HRE, slow degrading alloy from the family of WE-alloys (Rare earth base alloys) [44]. Additionally, Kawamura et al. (2020) reported undecalcified histology results with periosteal bone growth at 14 days in animals implanted with Mg-alloy and the presence of a fibrotic capsule around Ti implants at 14 and 30 days [45]. Titanium, while considered to be largely inert, may have contributed to increased tracer uptake levels compared to sham by a combination of factors: foreign body reaction causing the creation of fibrous capsule around it already on day 7 as observed in histology and reported

Table 6
Median SUVs and standard deviations by tracer, group and time point.

[^{18}F]FDG						
	Median			SD		
Day	Mg	Ti	Sham	Mg	Ti	Sham
1	26.31	23.65	18.60	5.97	5.92	4.25
3	30.76	31.76	19.41	7.25	7.13	7.92
7	26.32	22.01	0.00	7.78	4.90	0.00
14	14.55	13.89	9.72	3.86	2.38	3.68
28	11.80	12.99	8.69	3.18	3.52	2.43
45	9.68	14.36	7.75	3.46	4.37	2.33

[^{18}F]NaF						
	Median			SD		
Day	Mg	Ti	Sham	Mg	Ti	Sham
1	66.69	71.89	54.46	6.67	14.32	12.56
3	75.95	67.57	58.10	10.33	23.40	18.63
7	144.12	83.03	71.52	61.11	26.38	22.66
14	82.38	55.95	49.20	72.05	13.95	12.19
28	51.43	35.91	32.28	57.65	14.05	9.19
45	38.39	33.02	26.65	27.07	10.61	6.82

[^{68}Ga]NODAGA-RGD						
	Median			SD		
Day	Mg	Ti	Sham	Mg	Ti	Sham
7	4.75	5.04	5.62	0.59	0.84	0.52
15	4.53	4.78	2.93	0.84	0.45	0.24
32	2.87	3.65	2.52	0.45	0.63	0.19

previously, continuous damage to soft tissue during movement by the extended ends of the implant, osteoconductive effect of the titanium oxide layer [46–48], and press-fitted placement promoting gap healing between implant and bone surface [49]. Notably, the increase in SUV_{median} for [^{18}F]FDG for titanium group on day 45 (from 12.99 on day 28 to 14.36 on day 45, 10.02 % increase after steady decrease over previous time points) suggests chronic inflammatory response due to foreign body response. The histological evidence also suggests that the presence of implants may contribute to the elevated levels of [^{18}F]FDG and [^{18}F]NaF tracer uptake compared to sham injury due to the formation of callus around the point of contact of implant and bone surface.

Anti-inflammatory properties, often mentioned in other research, weren't observed with [^{18}F]FDG. This may be explained by the pro-inflammatory property of higher Mg^{+} concentration values [5] that has also been reported as non-cytotoxic and beneficial by acute stimulation of immune response promoting further angiogenesis and healing [6]. These effects would be expected to show a statistically significant increase in SUV between Mg and Ti groups also before day 7, which was not observed in this study. At the same time, the observed values on days 1–14 were generally higher for Mg group (SUV_{median} larger by 10.64 % on day 1, 17.83 % larger on day 7 and 4.64 % larger on day 14), with only on day 3 titanium implant group having median uptake values higher than magnesium group by 3.20 %. This can be explained by the accumulation of gas released in the process of magnesium corrosion creating voids near magnesium implants in soft tissues and medullary cavity, causing an underestimation of tracer uptake. Additionally, the histology of magnesium samples showed increased cellular activity that would lead to increased metabolism and FDG uptake. Sham injury could cause least observed uptake due to the defect remaining open, causing larger bleeding and haematoma, delaying the onset of healing. Also, the implant-long VOI in [^{18}F]FDG analysis may have in some sham group cases extended beyond the body, possibly causing an underestimation of the median uptake values.

At the same time, there is a distinct difference in peak SUV time point between two tracers: for all groups, [^{18}F]FDG uptake peaked on day 3, while the peak for [^{18}F]NaF uptake was on day 7. This corresponds to the results by Ben Amara et al. (2023), who reported peak inflammatory response for subcutaneous magnesium discs on day 3 [6]. [^{18}F]NaF uptake values culminating on day 7 are likely caused by the onset of osteoclast activity as the acute inflammatory stage was over and tissue healing was in progress. While also present to a lesser extent in [^{18}F]FDG results, from day 7 onwards, the magnesium group had multiple outliers showing significantly elevated SUVs for [^{18}F]NaF. Since these outliers belonged to the same animals, we hypothesise that these are a result of either damage caused during explantation due to the increased effort required to overcome the friction from reacting magnesium surface (thus requiring more healing to finish) or the animals moving before injury could stabilise. The latter hypothesis is supported by the fact that the outliers are not prominent on days 1 and 3, when animals are still likely to feel the aftereffects of the surgery. Such self-damaging behaviour is possibly linked to magnesium inhibiting calcium ions from entering cells by blocking N-methyl-d-aspartate (NMDA) receptors resulting in analgesic effect [50].

The pilot study with [^{68}Ga]NODAGA-RGD tracer had limited sample size to conduct statistical analysis, but the observed results provide interesting insight into peri–implant $\alpha_v\beta_3$ integrin expression. It is notable how in observed cases, SUVs in magnesium and titanium groups remained increased through days 7 and 15 (SUV_{median} change from 4.75 to 4.53, 4.74 % difference for Mg, from 5.04 to 4.78, 5.30 % difference for Ti) before the gradual obvious reduction at day 32 (on day 32, SUV_{median} for Mg = 2.87, 44.8 6 % reduction from day 14; for Ti day 32 SUV_{median} = 3.65, 23.93 % reduction from day 14). It is distinctly different from SUVs of sham injury group, which exhibited peak uptake on day 7 (SUV_{median} = 5.62), above implanted groups, before steep decrease on day 15 (SUV_{median} = 2.93, 62.92 % from day 7) with less change in uptake at day 32 (SUV_{median} = 2.52, 15.04 % change from day 15). The prolonged increase of $\alpha_v\beta_3$ expression in the presence of implants can be attributed to the damage of the adjacent blood vessels during movement, angiogenic properties of magnesium ions, vascularized capsule formation around implants (especially titanium) and osteoclast activity during bone remodelling in gap closure and callus formation that was observed in histology. Sham injury, due to the absence of implants, probably passed the peak angiogenesis and osteoclast expression stages before day 15, which also corresponds to the decrease in observed [^{18}F]FDG and [^{18}F]NaF uptake values in the period between days 7 and 14.

5. Conclusions

The use of PET-CT demonstrated good results in monitoring the tissue response and healing biomarkers between different groups. The observed differences confirm that PET-CT is a viable tool to study the metabolic effects of implant materials such as biodegradable metal alloys, an application previously largely unexplored.

A major limitation of the study analysis is a that the histological images were used only for qualitative assessment, and a very small sample size was allocated for this purpose. Without an advance understanding of the possible differences between groups, immunohistochemical analysis was not included. Since the focus of the study was on long-term imaging, following the principles of 3Rs (Replacement, Reduction and Refinement), we limited early time point sacrifices. One of the limitations of current study interpretation include uncertainty in the effects of voids caused by accumulated gas from magnesium degradation on tracer uptake quantification in the surrounding tissues. Another limitation is caused by the alternative binding targets of the tracers, such as [^{18}F]NaF uptake by dead bone. Furthermore, different implant ma-

terials, geometry, orientation and placement in combination with differences in correction algorithms and build of different imaging systems pose a challenge for standardisation of the technique.

While the heterogeneity of individual responses and radiological burden currently limit the application of the method in clinical routine, it is well suitable for preclinical research. After refining the approach and further studies with different tracers, this can be a potential method for quantitative evaluation of biological effects, promoting the development and assessment of biomaterials, especially biodegradable implants that need to be monitored over an extended period of time.

Declaration of competing interest

The authors declare that they have no known competing financial interests or personal relationships that could have appeared to influence the work reported in this paper.

CRediT authorship contribution statement

Leon Riehakainen: Writing – review & editing, Writing – original draft, Visualization, Methodology, Investigation, Conceptualization. **Eduarda Mota-Silva:** Writing – review & editing, Methodology, Investigation, Conceptualization. **Claudia Kusmic:** Writing – review & editing, Visualization, Supervision, Resources, Methodology. **Daniele Panetta:** Writing – review & editing, Supervision, Resources, Methodology. **Debora Petroni:** Resources. **Davide Fragnito:** Visualization, Formal analysis. **Stefano Salvadori:** Supervision, Formal analysis. **Luca Menichetti:** Writing – review & editing, Supervision, Resources, Methodology, Funding acquisition, Conceptualization.

Ethics approval and consent to participate

The animal experiments were performed in accordance with the National Ethical Guidelines (Italian Ministry of Health; D.L.vo 26/2014) and followed the guidelines from Directive 2010/63/EU of the European Parliament. The study protocol was approved by the Instituto Superiore di Sanità on behalf of the Italian Ministry of Health and Ethical Panel (Prot. n° 299/2020-PR) and the local ethics committee. The study was carried out in compliance with the ARRIVE guidelines. This article does not contain any studies with human participants.

Funding

The work at the IFC–CNR has received funding from the European Union Horizon 2020 Research and Innovation Programme with Marie Skłodowska-Curie Action 2018 (Project: MgSafe, Grant Agreement No. 811226).

Acknowledgements

We would like to thank Prof. Davide Caramella for reviewing the manuscript and Luca Serasini for his help with Graphical Abstract.

Availability of data and materials

The datasets generated during and/or analysed during the current study are available from the corresponding author on reasonable request.

Supplementary materials

Supplementary material associated with this article can be found, in the online version, at doi:10.1016/j.actbio.2024.06.005.

References

[1] X. Shen, P. Shukla, A review of titanium based orthopaedic implants (Part-I): physical characteristics, problems and the need for surface modification, Peen. Sci. Technol. 1 (2020) 301–332.
[2] J.S. Hayes, R.G. Richards, The use of titanium and stainless steel in fracture fixation, Expert Rev. Med. Devices 7 (6) (2010) 843–853, doi:10.1586/ERD.10.53.
[3] J. Walker, S. Shadanbaz, T.B.F. Woodfield, M.P. Staiger, G.J. Dias, Magnesium biomaterials for orthopedic application: a review from a biological perspective, *J. Biomed. Mater. Res. Part B* 102 (6) (2014) 1316–1331, doi:10.1002/JBM.B.33113.
[4] F. Witte, N. Hort, C. Vogt, S. Cohen, K.U. Kainer, R. Willumeit, F. Feyerabend, Degradable biomaterials based on magnesium corrosion, Curr. Opin. Solid State Mater. Sci. 12 (5–6) (2008) 63–72, doi:10.1016/J.COSSMS.2009.04.001.
[5] X. Zhang, Q. Chen, X. Mao, Magnesium enhances osteogenesis of BMSCs by tuning osteoimmunomodulation, Biomed Res. Int. 2019 (2019), doi:10.1155/2019/7908205.
[6] H. Ben Amara, D.C. Martinez, F.A. Shah, A.J. Loo, L. Emanuelsson, B. Norlindh, R. Willumeit-Römer, T. Plocinski, W. Swieszkowski, A. Palmquist, O. Omar, P. Thomsen, Magnesium implant degradation provides immunomodulatory and proangiogenic effects and attenuates peri-implant fibrosis in soft tissues, Bioact. Mater. 26 (2023) 353, doi:10.1016/J.BIOACTMAT.2023.02.014.
[7] S. Yoshizawa, A. Brown, A. Barchowsky, C. Sfeir, Magnesium ion stimulation of bone marrow stromal cells enhances osteogenic activity, simulating the effect of magnesium alloy degradation, Acta Biomater 10 (6) (2014) 2834–2842, doi:10.1016/J.ACTBIO.2014.02.002.
[8] F. Witte, The history of biodegradable magnesium implants: a review, Acta Biomater 6 (5) (2010) 1680–1692, doi:10.1016/J.ACTBIO.2010.02.028.
[9] P. Zhi, L. Liu, J. Chang, C. Liu, Q. Zhang, J. Zhou, Z. Liu, Y. Fan, Advances in the study of magnesium alloys and their use in bone implant material, Met. 2022 12 (9) (2022) 1500, doi:10.3390/MET12091500.
[10] G.E.J. Poinern, S. Brundavanam, D. Fawcett, Biomedical magnesium alloys: a review of material properties, surface modifications and potential as a biodegradable orthopaedic implant, Am. J. Biomed. Eng. 2 (6) (2012) 218–240, doi:10.5923/J.AJBE.20120206.02.
[11] V. Tsakiris, C. Tardei, F.M. Clicinschi, Biodegradable Mg alloys for orthopedic implants – a review, J. Magnes. Alloy. 9 (6) (2021) 1884–1905, doi:10.1016/J.JMA.2021.06.024.
[12] L. Riehakainen, C. Cavallini, P. Armanetti, D. Panetta, D. Caramella, L. Menichetti, In vivo imaging of biodegradable implants and related tissue biomarkers, Polymers 13 (14) (2021), doi:10.3390/POLYM13142348.
[13] W.K. Hsu, B.T. Feeley, L. Krenek, D.B. Stout, A.F. Chatziioannou, J.R. Lieberman, The use of 18F-fluoride and 18F-FDG PET scans to assess fracture healing in a rat femur model, Eur. J. Nucl. Med. Mol. Imaging 34 (8) (2007) 1291–1301, doi:10.1007/s00259-006-0280-6.
[14] C. Cyteval, A. Bourdon, Imaging orthopedic implant infections, Diagn. Interv. Imaging 93 (6) (2012) 547–557, doi:10.1016/j.diii.2012.03.004.
[15] M. Schiesser, K.D.M. Stumpe, O. Trentz, T. Kossmann, G.K. Von Schulthess, Detection of metallic implant–associated infections with FDG PET in patients with trauma: correlation with microbiologic results1, Radiology 226 (2) (2003) 391–398, doi:10.1148/RADIOL.2262011939.
[16] P.H. Brown, J.R. Carter, P. Moyade, M. Mohammed, M. De Matas, S. Vinjamuri, Real-world experience of the role of 18F FDG PET-computed tomography in chronic spinal implant infection, Nucl. Med. Commun. 41 (8) (2020) 715–720, doi:10.1097/MNM.0000000000001211.
[17] T. Falstie-Jensen, J. Lange, H. Daugaard, M.H. Vendelbo, A.K. Sørensen, B. Zerahn, J. Ovesen, K. Søballe, L.C. Gormsen, B.S. Olsen, H.V.S. Johanssen, B. Elmengaard, T.M. Thillemann, L. Bolvig, 18F FDG-PET/CT has poor diagnostic accuracy in diagnosing shoulder PJI, Eur. J. Nucl. Med. Mol. Imaging 46 (10) (2019) 2013–2022, doi:10.1007/S00259-019-04381-W.
[18] R.M. Kwee, T.C. Kwee, 18F-FDG PET for diagnosing infections in prosthetic joints, PET Clin. 15 (2) (2020) 197–205, doi:10.1016/J.CPET.2019.11.005.
[19] M. Beheshti, F.M. Mottaghy, F. Payche, F.F.F. Behrendt, T. Van den Wyngaert, I. Fogelman, K. Strobel, M. Celli, S. Fanti, F. Giammarile, B. Krause, W. Langsteger, (18)F-NaF PET/CT: EANM procedure guidelines for bone imaging, Eur. J. Nucl. Med. Mol. Imaging 42 (11) (2015) 1767–1777, doi:10.1007/S00259-015-3138-Y.
[20] F. Cofano, D. Armocida, L. Ruffini, M. Scarlattei, G. Baldari, G. Di Perna, G. Pilloni, F. Zenga, E. Ballante, D. Garbossa, F. Tartara, The efficacy of trabecular titanium cages to induce reparative bone activity after lumbar arthrodesis studied through the 18f-Naf PET/CT scan: observational clinical in-vivo study, Diagnostics 12 (10) (2022), doi:10.3390/DIAGNOSTICS12102296.
[21] M. Blau, R. Ganatra, M.A. Bender, 18F-fluoride for bone imaging, Semin. Nucl. Med. 2 (1) (1972) 31–37, doi:10.1016/S0001-2998(72)80005-9.
[22] M. Bernhardsson, O. Sandberg, M. Ressner, J. Koziorowski, J. Malmquist, P. Aspenberg, Shining dead bone—cause for cautious interpretation of [18F]NaF PET scans, Acta Orthop 89 (1) (2018) 124–127, doi:10.1080/17453674.2017.1372097.
[23] P.C. Brooks, R.A.F. Clark, D.A. Cheresh, Requirement of vascular integrin $\alpha v\beta 3$ for angiogenesis, Science 264 (5158) (1994) 569–571, doi:10.1126/SCIENCE.7512751.
[24] T. Rasmussen, B. Follin, J. Kastrup, M. Brandt-Larsen, J. Madsen, T. Emil Christensen, M. Juhl, S. Cohen, K. Pharao Hammelev, C. Holdflod Møller, J. Peter Goetze, P. Hasbak, A. Kjaer, S. Goldstein-Goren, Angiogenesis PET tracer uptake (68 Ga-NODAGA-E[(cRGDyK)] 2) in induced myocardial infarction and stromal cell treatment in minipigs, Diagnostics 8 (2018) 33, doi:10.3390/diagnostics8020033.

[25] M. Grönman, M. Tarkia, T. Kiviniemi, P. Halonen, A. Kuivanen, T. Savunen, T. Tolvanen, J. Teuho, M. Käkelä, O. Metsälä, M. Pietilä, P. Saukko, S. Ylä-Herttuala, J. Knuuti, A. Roivainen, A. Saraste, Imaging of $\alpha v\beta 3$ integrin expression in experimental myocardial ischemia with [68Ga]NODAGA-RGD positron emission tomography, J. Transl. Med. 15 (1) (2017) 1–11, doi:10.1186/S12967-017-1245-1/FIGURES/6.
[26] W. Nammas, C. Paunonen, J. Teuho, P. Luoto, M. Kakela, A. Hietanen, T. Viljanen, X.-G. Li, A. Roivainen, J. Knuuti, A. Saraste, Molecular imaging of alphaVbeta3 integrin for evaluation of myocardial injury after acute myocardial infarction, Eur. Heart J. 43 (Supplement_2) (2022), doi:10.1093/EURHEARTJ/EHAC544.322.
[27] R.A.F. Clark, M.G. Tonnesen, J. Gailit, D.A. Cheresh, Transient functional expression of alphaVbeta 3 on vascular cells during wound repair, Am. J. Pathol. 148 (5) (1996) 1407.
[28] M.A. Horton, E.L. Dorey, S.A. Nesbitt, J. Samanen, F.E. Ali, J.M. Stadel, A. Nichols, R. Greig, M.H. Helfrich, Modulation of vitronectin receptor-mediated osteoclast adhesion by Arg-Gly-Asp peptide analogs: a structure-function analysis, J. Bone Miner. Res. 8 (2) (1993) 239–247, doi:10.1002/JBMR.5650080215.
[29] C. Rațiu, A.B. Boșca, A. Ilea, F. Ruxanda, V. Miclăuș, Osteoclast recruitment and polymorphism during the healing process in dental implant surgery, Rom. Biotechnol. Lett. 24 (1) (2019) 66–74, doi:10.25083/RBL/24.1/66.74.
[30] M.I. Hofstee, G. Muthukrishnan, G.J. Atkins, M. Riool, K. Thompson, M. Morgenstern, M.J. Stoddart, R.G. Richards, S.A.J. Zaat, T.F. Moriarty, Current concepts of osteomyelitis: from pathologic mechanisms to advanced research methods, Am. J. Pathol. 190 (6) (2020) 1151–1163, doi:10.1016/J.AJPATH.2020.02.007.
[31] D. Savio, A. Bagno, When the total hip replacement fails: a review on the stress-shielding effect, Process. 2022 10 (3) (2022) 612, doi:10.3390/PR10030612.
[32] T.H.J. Nijhuis, S.A.S. de Boer, A.L. Wahegaonkar, A.T. Bishop, A.Y. Shin, S.E.R. Hovius, R.W. Selles, A new approach to assess the gastrocnemius muscle volume in rodents using ultrasound; comparison with the gastrocnemius muscle index, PLoS ONE 8 (1) (2013), doi:10.1371/JOURNAL.PONE.0054041.
[33] N. Belcari, N. Camarlinghi, S. Ferretti, P. Iozzo, D. Panetta, P.A. Salvadori, G. Sportelli, A. Del Guerra, NEMA NU-4 performance evaluation of the IRIS PET/CT preclinical scanner, IEEE Trans. Radiat. Plasma Med. Sci. 1 (4) (2017) 301–309, doi:10.1109/TRPMS.2017.2707300.
[34] D. Panetta, N. Belcari, M. Tripodi, S. Burchielli, P.A. Salvadori, A. Del Guerra, Performance evaluation of the CT component of the IRIS PET/CT preclinical tomograph, Nucl. Instruments Methods Phys. Res. Sect. A 805 (2016) 135–144, doi:10.1016/J.NIMA.2015.08.044.
[35] K. Ravindra, P. Rattan, S. Mor, A.N. Aggarwal, Generalized additive models: building evidence of air pollution, climate change and human health, Environ. Int. 132 (2019) 104987, doi:10.1016/J.ENVINT.2019.104987.
[36] M. Wieling, Analyzing dynamic phonetic data using generalized additive mixed modeling: a tutorial focusing on articulatory differences between L1 and L2 speakers of English, J. Phon. 70 (2018) 86–116, doi:10.1016/J.WOCN.2018.03.002.
[37] Y. Benjamini, Y. Hochberg, Controlling the false discovery rate: a practical and powerful approach to multiple testing, J. R. Stat. Soc. Ser. B 57 (1) (1995) 289–300, doi:10.1111/J.2517-6161.1995.TB02031.X.
[38] C. Castellani, R.A. Lindtner, P. Hausbrandt, E. Tschegg, S.E. Stanzl-Tschegg, G. Zanoni, S. Beck, A.M. Weinberg, Bone-implant interface strength and osseointegration: biodegradable magnesium alloy versus standard titanium control, Acta Biomater. 7 (1) (2011) 432–440, doi:10.1016/J.ACTBIO.2010.08.020.
[39] F. Amerstorfer, S.F. Fischerauer, L. Fischer, J. Eichler, J. Draxler, A. Zitek, M. Meischel, E. Martinelli, T. Kraus, S. Hann, S.E. Stanzl-Tschegg, P.J. Uggowitzer, J.F. Löffler, A.M. Weinberg, T. Prohaska, Long-term in vivo degradation behavior and near-implant distribution of resorbed elements for magnesium alloys WZ21 and ZX50, Acta Biomater. 42 (2016) 440–450, doi:10.1016/J.ACTBIO.2016.06.025.
[40] T. Kraus, S. Fischerauer, S. Treichler, E. Martinelli, J. Eichler, A. Myrissa, S. Zötsch, P.J. Uggowitzer, J.F. Löffler, A.M. Weinberg, The influence of biodegradable magnesium implants on the growth plate, Acta Biomater. 66 (2018) 109–117, doi:10.1016/J.ACTBIO.2017.11.031.
[41] J. Mosier, N. Nguyen, K. Parker, C. LaShanSimpson, J. Mosier, N. Nguyen, K. Parker, C. LaShanSimpson, Calcification of biomaterials and diseased states, Biomater. Phys. Chem. New Ed. (2017), doi:10.5772/INTECHOPEN.71594.
[42] Q. Liu, Z. Wang, X. Dong, H. Wang, J. Lan, Calcium, phosphorus and oxygen around implant at early osseointegration in hyperlipidemic rats, J. Hard Tissue Biol. 28 (1) (2019) 57–62, doi:10.2485/JHTB.28.57.
[43] B. Okutan, U.Y. Schwarze, L. Berger, D.C. Martinez, V. Herber, O. Suljevic, T. Plocinski, W. Swieszkowski, S.G. Santos, R. Schindl, J.F. Löffler, A.M. Weinberg, N.G. Sommer, The combined effect of zinc and calcium on the biodegradation of ultrahigh-purity magnesium implants, Biomater. Adv. 146 (2023) 213287, doi:10.1016/J.BIOADV.2023.213287.
[44] R.A. Lindtner, C. Castellani, S. Tangl, G. Zanoni, P. Hausbrandt, E.K. Tschegg, S.E. Stanzl-Tschegg, A.M. Weinberg, Comparative biomechanical and radiological characterization of osseointegration of a biodegradable magnesium alloy pin and a copolymeric control for osteosynthesis, J. Mech. Behav. Biomed. Mater. 28 (2013) 232–243, doi:10.1016/J.JMBBM.2013.08.008.
[45] N. Kawamura, Y. Nakao, R. Ishikawa, D. Tsuchida, M. Iijima, Degradation and biocompatibility of AZ31 magnesium alloy implants in vitro and in vivo: a micro-computed tomography study in rats, Mater. 13 (2) (2020), doi:10.3390/MA13020473.
[46] A. Smieszek, A. Seweryn, K. Marcinkowska, M. Sikora, K. Lawniczak-Jablonska, B.S. Witkowski, P. Kuzmiuk, M. Godlewski, K. Marycz, Titanium dioxide thin films obtained by atomic layer deposition promotes osteoblasts' viability and differentiation potential while inhibiting osteoclast activity-potential application for osteoporotic bone regeneration, Mater 13 (21) (2020) 1–20, doi:10.3390/MA13214817.
[47] M.K. Le Thieu, S. Stoetzel, M. Rahmati, T. El Khassawna, A. Verket, J. Sanz-Esporrin, M. Sanz, J.E. Ellingsen, H.J. Haugen, Immunohistochemical comparison of lateral bone augmentation using a synthetic TiO2 block or a xenogeneic graft in chronic alveolar defects, Clin. Implant Dent. Relat. Res. 25 (1) (2023) 57–67, doi:10.1111/CID.13143.
[48] A. Asserghine, D. Filotás, L. Nagy, R.M. Souto, G. Nagy, Do titanium biomaterials get immediately and entirely repassivated? A perspective, npj Mater. Degrad. 6 (1) (2022) 1–5, doi:10.1038/s41529-022-00270-0.
[49] P.J. Muire, L.H. Mangum, J.C. Wenke, Time course of immune response and immunomodulation during normal and delayed healing of musculoskeletal wounds, Front. Immunol. 11 (2020) 1056, doi:10.3389/FIMMU.2020.01056.
[50] H.J. Shin, H.S. Na, S.H. Do, Magnesium and pain, Nutrients 12 (8) (2020) 1–13, doi:10.3390/NU12082184.